Navier–Stokes Predictions of Pitch Damping for Axisymmetric Projectiles

Paul Weinacht[*] and Walter B. Sturek[†]
U.S. Army Research Laboratory, Aberdeen Proving Ground, Maryland 21005
and
Lewis B. Schiff[‡]
NASA Ames Research Center, Moffett Field, California 94035

An approach for predicting the pitch-damping coefficient sum for axisymmetric flight bodies is presented. The approach utilizes a specific combination of spinning and coning motions that allows the pitch-damping force and moment coefficient to be directly related to the aerodynamic side force and moment. The use of combined spinning and coning motion represents an improvement over existing techniques that utilize lunar coning motion for predicting the pitch-damping coefficients. A parabolized Navier–Stokes approach that utilizes a missile-fixed, noninertial rotating coordinate frame is applied to predict the flowfields about axisymmetric projectiles undergoing steady coning motion. The governing equations are modified to include the centrifugal and Coriolis force terms due to the rotating coordinate frame. From the computed flowfield, the side force and moment due to coning motion, spinning motion, and combined spinning and coning motion are used to determine the pitch-damping coefficients. Computations are performed for a generic shell configuration (with and without boattail), and the predictions show good agreement with an existing inviscid code. The comparisons of computational results for a family of ogive-cylinder configurations with aerodynamics range data show excellent agreement and further validate the approach.

Nomenclature

a	= speed of sound
C_m	= pitching moment coefficient
$C_{m_q} + C_{m_{\dot\alpha}}$	= pitch-damping moment coefficient
C_{m_α}	= slope of the pitching moment coefficient with angle of attack
$C_{N_q} + C_{N_{\dot\alpha}}$	= pitch-damping force coefficient
C_{N_α}	= slope of the normal force coefficient with angle of attack
C_n	= side moment coefficient
$C_{n_{p\alpha}}$	= Magnus moment coefficient
$C_{n_{\dot\phi}}$	= slope of the side moment coefficient with coning rate
D	= projectile diameter
$\hat{E}, \hat{F}, \hat{G}$	= inviscid flux vectors in transformed coordinates
e	= total energy per unit volume, nondimensionalized by $\rho_\infty a_\infty^2$
$\hat{H}$	= source term resulting from rotating coordinate frame
J	= Jacobian
L	= projectile body length
l	= characteristic length, typically the projectile diameter
M_∞	= freestream Mach number
P	= pressure, as used in thin-layer Navier–Stokes equations, nondimensionalized by $\rho_\infty a_\infty^2$
Pr	= Prandtl number
Pr_t	= turbulent Prandtl number
p	= spin rate in nonrolling coordinate frame, as used in the aerodynamic moment equations and coefficients
Re	= Reynolds number, $a_\infty \rho_\infty D / \mu_\infty$
r	= radial coordinate, nondimensionalized by D
$\hat{S}$	= viscous flux vector in transformed coordinates
s	= distance downrange
s_{cg}	= center of gravity shift, calibers
t	= time
U, V, W	= contravariant velocities of the transformed Navier–Stokes equations
u, v, w	= velocity components in x, y, and z directions, nondimensionalized by a_∞
V	= freestream velocity used to nondimensionalize the coning rate, spin rate, and aerodynamic coefficients
x, y, z	= axial, horizontal, and vertical coordinates with respect to the body
x_{cg}	= axial location of projectile center of gravity with respect to the axial coordinate x
α	= vertical component of angle of attack in nonrolling coordinates
α_t	= total angle of attack, $\sqrt{(\alpha^2 + \beta^2)}$
β	= horizontal component of angle of attack in nonrolling coordinates
γ	= ratio of specific heats, as used in Navier–Stokes equations; cosine of the total angle of attack, as used in aerodynamic force and moment formulations
δ	= sine of the total angle of attack
μ	= laminar viscosity
μ_t	= effective turbulent eddy viscosity
ξ, η, ζ	= transformed coordinates in Navier–Stokes equations
$\tilde{\xi}$	= complex quantity representing the components of the sine of the angle of attack with respect to the nonrolling coordinate frame
ρ	= density, normalized by ρ_∞
ϕ	= circumferential coordinate as measured from vertical axis
$\dot{\phi}$	= coning rate of projectile
$\dot{\phi}D/V$	= nondimensional coning rate
Ω_c	= coning rate of projectile, nondimensionalized by a_∞/D
ω	= spin rate in coning reference frame

Introduction

PREDICTION of the in-flight motion of projectiles requires the determination of the aerodynamic forces and moments that act on the body. These aerodynamic forces and moments may be determined by experimental or theoretical means, such as computational fluid dynamics (CFD). From a computational standpoint, much of the research effort has focused on determining the static aerodynamics such as drag and pitching moment. Only a limited number of studies have focused on numerical prediction of dynamic aerodynamic derivatives such as pitch-damping force and moment. In the current research effort, a parabolized Navier–Stokes (PNS) technique has been adapted to predict the pitch-damping force and moment using steady coning motion.

By applying linear flight mechanics theory, e.g., Ref. 1, it can be shown that aerodynamic side force and moment coefficients acting on a projectile in steady coning motion can be related to the pitch-damping force and moment coefficients. In steady coning motion, the longitudinal axis of the missile performs a rotation at a constant angular velocity about a line parallel to the freestream velocity vector and coincident with the projectile center of gravity (c.g.), while oriented at a constant angle with respect to the freestream velocity vector, as schematically shown in Fig. 1. The use of steady coning motion to determine the pitch-damping aerodynamic coefficients provides an interesting and cost-effective approach for determining the aerodynamics that are normally associated with unsteady or time-dependent motions.

Previously, Tobak et al.[2] examined the aerodynamics of bodies of revolution in coning motion and proposed that the nonlinear aerodynamic forces and moments acting on a body performing large amplitude nonplanar motions could be composed of four characteristic motions: 1) steady angle of attack, 2) pitching motion, 3) rolling motion, and 4) coning motion. Typically, the linear aerodynamic force and moment formulation considers only forces and moments due to the first three motions and assumes that a nonplanar motion can be described by the vector sum of two independent planar motions. The addition of coning motion allows for coupling between planar motions in the nonlinear formulation. Their nonlinear theory[2] also confirms the linear theory result that the side force and moment due to coning motion is related to the linear pitch-damping coefficients.

To provide additional validation for the theory, Schiff and Tobak[3] performed wind-tunnel experiments on a conical body undergoing separate or combined spinning and coning motions. Their results showed that, at low angles of attack, the slopes of the side force and moment with angle of attack normalized by the coning rate were in good agreement with predictions of the damping-in-pitch force and moment coefficients obtained using linearized theory. They also demonstrated that the Magnus force and moment (variation of side force and moment with spin rate and angle of attack) was small; thus, the linear pitch-damping coefficients could be determined from the side force and moment due to coning alone.

Subsequently, Schiff[4] computed the supersonic inviscid flow about a conical body undergoing coning motion. To compute the flow around the body in coning motion, Schiff made use of a rotating coordinate frame. Within the rotating coordinate frame, the flow was steady; thus, the steady Euler equations could be solved. The governing equations were modified to include the centrifugal and Coriolis force terms. His computed results[4] compared well with experimental results and with estimates of pitch-damping coefficients using a linear theory. Later studies by other researchers also employed rotating coordinate frames to compute the supersonic viscous flow about conical bodies in coning motion.[5,6] More recently, computations for finned projectiles in coning motion[7] were performed to determine the pitch-damping coefficients.

In each of the previous efforts, the pitch-damping coefficients were determined from the side moment due to steady lunar coning motion, which required the Magnus moment to be neglected. The predictions of the pitch-damping coefficients presented in this paper were determined from the side moment due to a specific combination of spinning and coning motion, which allows the side moment due to this motion to be directly related to the pitch-damping force and moment coefficients. These motions will be defined in more detail in the next section.

In the current paper, predictions of pitch-damping for an axisymmetric shell were made using combined spinning and coning motions. The flowfield about these projectiles in steady coning motion has been successfully computed using a PNS computational approach.[8] The computations are performed in a rotating coordinate frame similar to that employed originally by Schiff.[4] Code modification required to implement the rotating coordinate frame, including the addition of the centrifugal and Coriolis source terms and changes to the shock-fitting algorithm, are discussed. From the computed flowfield, the side moments due to coning motion, spinning motion, and combined spinning and coning motion are used to determine the pitch-damping coefficient. Computations have been performed for two generic shell configurations, a secant-ogive-cylinder (SOC) and a secant-ogive-cylinder-boattail (SOCBT) configuration. The PNS predictions are made for various length-to-diameter ratios and supersonic Mach numbers and are compared with predictions made using a previously reported Euler code.[4] Results are also presented for a series of ogive-cylinder configurations that have been fired through an aerodynamics range located at the former U.S. Army Ballistic Research Laboratory (now part of the U.S. Army Research Laboratory). Comparisons between PNS results and range data are made.

Theoretical Background

In this section, the moment expansion of a symmetric missile is first introduced. Two types of coning motion are described and related to the pitching motion of the missile body. Finally, the moments produced by both types of coning motion are related to the various moment components in the moment expansion. In particular, the pitch-damping moment is related to the side moment due to coning motion.

Moment Expansion

It is common in aeroballistic applications to utilize a missile-fixed, nonrolling coordinate system to describe both the kinematics and the system of forces and moments that act on the projectile in flight.[1] The nonrolling coordinate system affords some simplifications, particularly in describing the kinematics. In this paper, the primary reason for initially describing the aerodynamic moments using the nonrolling coordinate system is that the description is well established. The nonrolling coordinate frame is an orthogonal right-handed system $(\tilde{x}, \tilde{y}, \tilde{z})$ centered at the body c.g. The $\tilde{x}$ axis is aligned along the projectile longitudinal axis with the positive direction oriented toward the projectile nose. The $\tilde{z}$ axis is initially oriented downward with the $\tilde{x}$–$\tilde{z}$ plane perpendicular to the ground. The angular motion of the nonrolling coordinate frame is such that, with respect to an inertial frame, the $\tilde{x}$ component of the coordinate frame's angular velocity is zero. Although the time-dependent orientation of the nonrolling frame may be hard to visualize, the nonrolling frame is essentially equivalent to the fixed-plane coordinate system for small amplitude motions. In the fixed-plane coordinate system, the $\tilde{x}$–$\tilde{z}$ plane remains perpendicular to the ground for all time. Further details on these coordinate frames can be found in Ref. 1.
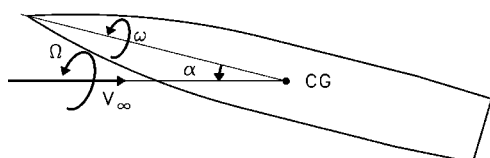

Fig. 1   Schematic of coning motion.

The moment expansion[1] for a symmetric missile in the nonrolling coordinate frame is

$$\tilde{C}_m + i\tilde{C}_n = \left[(pl/V)C_{n_{p\alpha}} - iC_{m_\alpha}\right]\tilde{\boldsymbol{\xi}} - (i/\gamma)\left[C_{m_q} + \gamma C_{m_{\dot\alpha}}\right]\tilde{\boldsymbol{\xi}}'$$

(1)

The moment formulation uses complex variables to separate the moment components, $\tilde{C}_m$ and $\tilde{C}_n$, that are oriented along the $\tilde{y}$ and $\tilde{z}$ axes, respectively. The third moment component, the roll moment, can be handled separately and is not of consequence in this study.

In the moment expansion, the pitching moment coefficient slope C_{m_α} and pitch-damping moment coefficient $C_{m_q} + \gamma C_{m_{\dot\alpha}}$ produce moments that are proportional to the complex yaw $\tilde{\boldsymbol{\xi}}$ and yawing rate $\tilde{\boldsymbol{\xi}}'$, respectively. (In the analysis presented, there is no need to distinguish between pitch and yaw and the terms may be interchanged. The usage follows that of Murphy.[1]) The Magnus moment coefficient $C_{n_{p\alpha}}$ accounts for a side moment due to flow asymmetries from a combination of spin and angle of attack.

Experimental procedures to determine both the pitching and Magnus moments are conceptually easy to devise because these moments depend on the angle of attack and not the angular rate. For instance, the pitching and Magnus moments can be determined from wind-tunnel measurements of pitch-plane and side moments on a spinning flight body held at a fixed angle of attack. Because this is a steady motion for axisymmetric bodies, computational analogs based on steady flow techniques can be easily implemented. In contrast, the pitch-damping moment is produced by the angular rate, which seems to imply that a time-dependent motion is required to produce the moment. One obvious unsteady motion that might be considered is a planar constant amplitude pitching motion. Experiments and computational approaches can be devised to determine the pitch-damping moment from unsteady motions, but this may be an unnecessary complication. It is possible to devise motions that still produce an angular rate, but when viewed in the appropriate coordinate system, are steady motions. Coning motion represents one such motion.

Relation Between Coning and Pitching Motions

As was discussed earlier, in steady coning motion, the longitudinal axis of the missile performs a rotation at a constant angular velocity about a line parallel to the freestream velocity vector and coincident with the projectile c.g. while oriented at a constant angle with respect to the freestream velocity vector. The motion is shown schematically in Fig. 1. In this context, coning motion also requires the c.g. to traverse a rectilinear path at constant velocity. With respect to the nonrolling coordinate frame, the vertical and horizontal components of the angle of attack, α and β, vary in a periodic fashion as the projectile rotates about the freestream velocity vector. However, the total angle of attack, $\alpha_t \approx \sqrt{(\alpha^2 + \beta^2)}$, is constant.

Both of these components of the angle of attack, when plotted as a function of time, are sinusoidal, constant amplitude pitching motions that are out of phase with each other by one-quarter of a cycle. By decomposing coning motion in this fashion, it can be observed that coning motion contains a specific linear combination of two orthogonal planar pitching motions. As will be shown later, this particular combination of planar pitching motions yields a nonzero angular rate, which is a requirement for producing the pitch-damping moment.

The phrase "steady coning motion" describes the rotation of the longitudinal axis of the body about the freestream velocity vector but does not completely describe the motion of the body. In particular, the projectile may rotate (or spin) about its longitudinal axis. Two particular forms of coning motion, steady lunar coning motion and steady combined spinning and coning motion, are utilized. The two motions differ in their treatment of the angular velocity about the longitudinal axis.

In steady lunar coning motion, the angular velocity of the projectile results purely from the rotation of the projectile about the freestream velocity vector. The angular velocity of the projectile includes a component along the projectile's longitudinal axis, which by definition is the spin rate of the projectile in the nonrolling coordinate system. The relation between spin rate p and coning rate $\dot\phi$ for the case of steady lunar coning motion is

$$p = \dot\phi \cos \alpha_t = \dot\phi \gamma$$

(2)

In steady combined spinning and coning motion, the angular velocity of the projectile consists of the vector sum of two angular velocity vectors. The first vector produces a rotation of the projectile's longitudinal axis about the freestream velocity vector (coning motion) $\dot\phi$, and the second produces a rotation of the projectile about its longitudinal axis (spinning motion) ω. In general, there is no requirement for the spin rate to be coupled to the coning rate. However, in this context, combined spinning and coning motion requires that ω be equal in magnitude but opposite in sign to the component of $\dot\phi$ along the longitudinal axis, $\omega = -\dot\phi \cos \alpha_t$. In this case, the total angular velocity of the body about the longitudinal axis is zero; hence, the spin rate in the nonrolling coordinate system is zero:

$$p = 0$$

(3)

By specifying both the coning rate and the spin rate, the projectile angular motion is now completely defined. For the particular case of steady lunar coning, the motion can be decomposed into a combination of two orthogonal planar pitching motions, plus a spinning motion at angle of attack. Likewise, steady combined spinning and coning motion can be decomposed into two orthogonal pitching motions.

Planar pitching motion is clearly a time-dependent motion that produces a time-dependent flowfield about the projectile. Steady lunar coning motion, on the other hand, should produce a steady flowfield when viewed from the appropriate coordinate frame, such as the coning coordinate frame. In the coning frame, the x axis is aligned with the longitudinal axis of the missile and is identical to the $\tilde{x}$ axis in the nonrolling frame. The plane formed by the x axis and z axis in the coning frame is parallel to the pitch plane. The y axis is oriented normal to the pitch plane so that an orthogonal right-handed coordinate system is formed.

For steady lunar coning motion, the coning frame and the body rotate at the same angular velocity; thus, there is no rotation of the pitch plane with respect to the body. Because the boundary conditions in the coning frame do not introduce any time dependency into the problem, when observed from the coning reference frame, the resulting flowfield is expected to be steady for small angles of attack and for small coning rates. It is important to realize that because the coning frame is rotating at a constant angular velocity and because the body does not rotate with respect to the coning frame of reference, there is no requirement for the body to have any special forms of geometric symmetry, i.e., axisymmetry, for steady flow to exist. Steady flow modeling techniques can be applied to determine the flowfield due to steady lunar coning motion under the constraints that both the coning rate and the angle of attack are small. (Clearly, the flow may become unsteady at high coning rates or high angles of attack, in much the same way the flow over a body at fixed angle of attack at high incidence can become unsteady due to vortex shedding.)

For the case of steady combined spinning and coning motion, the body will rotate in the coning reference frame with a rate of rotation, which is proportional to the coning rate, $(\omega = -\dot\phi \cos \alpha_t)$. This rotation does not produce a time-dependent boundary condition for axisymmetric bodies, and a steady flowfield can exist. However, for nonaxisymmetric bodies, the rotation of the body in the coning reference frame will produce a time-dependent (periodic) boundary condition and flowfield. Thus, when combined spinning and coning motion is utilized, a steady flowfield is only possible for axisymmetric bodies.

The steady nature of the flow in the coning frame makes the coning frame a desirable coordinate system for performing the fluid dynamic computations. Because the coning reference frame is a noninertial system due to the rotation of the coordinate system, the governing equations for the fluid dynamics must be modified. Further details on the implementation of the rotating frame are provided in the discussion of the computational approach.

Relation Between Side Moment Due to Coning and Pitch-Damping Moment

To develop the relation between the side moment due to coning motion and the pitch-damping moment coefficient, it is convenient

to resolve the moment components in nonrolling coordinates into moment components in the coning coordinate frame. The relationship between the transverse moments in the nonrolling frame and the coning frame, as well as the relations for the complex angle of attack and angular rate are shown in Eq. (4). These relations, valid for steady coning motion, have been simplified from the general case of arbitrary motion[9]:

$$C_m + iC_n = ie^{-i\gamma\dot{\phi}t}(\tilde{C}_m + i\tilde{C}_n) \qquad \tilde{\xi} = \delta e^{i\gamma\dot{\phi}t}$$
(4)

$$\tilde{\xi}' \equiv \frac{d\tilde{\xi}}{d(s/l)} = i\delta\gamma\frac{\dot{\phi}l}{V}e^{i\gamma\dot{\phi}t}$$

The moment formulation cast in terms of the in-plane and side moments can be written as follows:

$$C_m + iC_n = C_{m\alpha}\delta + i\left\{(pl/V)C_{np\alpha}\delta + \delta(\dot{\phi}l/V)\left[C_{m_q} + \gamma C_{m\dot{\alpha}}\right]\right\}$$
(5)

The resulting expression for the in-plane and side moments is independent of time for the case of steady coning and spinning motions. The in-plane moment (real part) results only from the pitching moment, whereas the total side moment (complex part) consists of contributions from the Magnus moment and pitch-damping moment. For the two types of coning motion of interest, the side moment assumes a particular form depending on the spin rate.

Side Moment for Lunar Coning Motion
As already discussed, with respect to the nonrolling coordinate system, lunar coning motion produces a component of angular velocity along the longitudinal axis of the missile, which by definition is the spin rate of the projectile [Eq. (2)]. For this type of coning motion, the side moment can be written as

$$C_n = \delta(\dot{\phi}l/V)\left(\gamma C_{np\alpha} + \left[C_{m_q} + \gamma C_{m\dot{\alpha}}\right]\right)$$
(6)

The notation can be simplified by noting that the right-hand side (RHS) of Eq. (6) is simply the variation of side moment with coning rate, valid for linear variations of side moment with coning rate,

$$C_{n_{\dot{\phi}}} \equiv \frac{\partial C_n}{\partial(\dot{\phi}l/V)} = \delta\left(\gamma C_{np\alpha} + \left[C_{m_q} + \gamma C_{m\dot{\alpha}}\right]\right)$$
(7)

This relation is identical to that presented by Schiff and Tobak[3] for bodies of revolution. Equation (7) relates the variation of the side moment with coning rate $C_{n_{\dot{\phi}}}$ to the pitch-damping coefficient $[C_{m_q} + \gamma C_{m\dot{\alpha}}]$ and the Magnus moment coefficient $C_{np\alpha}$. Assuming that $C_{n_{\dot{\phi}}}$ and $C_{np\alpha}$ can be determined, this relation will allow the pitch-damping coefficient to be determined.

Despite the fact that lunar coning motion requires that $C_{np\alpha}$ be determined (or assumed negligible) to determine the pitch-damping coefficient, this motion is useful. Because the body does not rotate with respect to the pitch plane while undergoing coning motion, the flow, when observed in the coning coordinate frame, will be steady for axisymmetric and nonaxisymmetric bodies. In many cases, particularly in supersonic flow, $C_{np\alpha}$ may be neglected without any appreciable loss of accuracy. This approach has been recently applied to predict the pitch damping for six-finned projectiles.[7] Note that nonaxisymmetric bodies with aerodynamic coefficients that exhibit a significant dependence on roll angle may need to be treated with a more general aerodynamic formulation[10,11] than is presented here.

Side Moment for Combined Spinning and Coning Motion
The second type of coning motion uses a specific combination of coning and spinning motions to cause the component of the total angular velocity along the longitudinal axis of the missile to be zero. In other words, both the nonrolling coordinate frame and a body fixed coordinate frame will not rotate with respect to each other. Thus, the spin rate of the projectile, as observed from the nonrolling coordinates, is zero [Eq. (3)].

Note, however, that the coning coordinate frame rotates with respect to the nonrolling coordinate frame and the body-fixed coordinate frame. In the coning coordinate frame, then, the body appears to perform a spinning motion because the body-fixed coordinate system rotates with respect to the coning coordinate frame. The spin rate in the coning coordinate frame will be $\omega = -\gamma\dot{\phi}$. This motion is called combined spinning and coning motion, because in the coning frame (which is the coordinate frame in which the computations are performed) the motion is a specific combination of spinning and coning motion. In the coning frame, this motion is a steady motion for axisymmetric bodies only. The presence of spin and angle of attack produce a periodic motion for nonaxisymmetric bodies, thereby eliminating steady flow computational approaches from consideration.

For this type of coning motion, the side moment can be written as

$$C_n = \delta(\dot{\phi}l/V)\left[C_{m_q} + \gamma C_{m\dot{\alpha}}\right]$$
(8)

In this case, the side moment is directly proportional to the pitch-damping moment coefficient. In contrast to side moment due to lunar coning motion [Eq. (6)], no Magnus moment term appears here. Despite the simplicity of this expression, the Magnus effect has not been entirely removed from the problem. In the coning frame, the combination of angle of attack from the coning motion and the spinning motion produce a Magnus-like effect. Thus, any approach, whether it be computational or experimental, that uses this motion must be capable of modeling both of these effects. For example, a coarse grid CFD computation that does not resolve the viscous effects sufficiently to properly model the Magnus problem will produce pitch-damping results that will be in error by the degree to which $C_{np\alpha}$ is improperly determined.

Side Force due to Coning Motions
Similar expressions relating side force due to coning to the pitch-damping force coefficient can be developed using the same approach used in analyzing the moments. The resulting expressions for the side force coefficients are similar in form to the expressions for the corresponding side moment coefficients for both types of motions.

For the case of lunar coning motion, the slope of the side force with coning rate $C_{Y_{\dot{\phi}}}$ is a function of the pitch-damping force coefficient $C_{N_q} + \gamma C_{N\dot{\alpha}}$ and the Magnus force coefficient $C_{Yp\alpha}$:

$$C_{Y_{\dot{\phi}}} = \delta\left(\gamma C_{Yp\alpha} + \left[C_{N_q} + \gamma C_{N\dot{\alpha}}\right]\right)$$
(9)

Like the side moment due to lunar coning motion, determining the pitch-damping force coefficient from the side force due to lunar coning requires that the Magnus term be ignored or determined from another source.

For combined spinning and coning motion, the slope of the side force with coning rate $C_{Y_{\dot{\phi}}}$ can be directly related to the pitch-damping force coefficient $C_{N_q} + \gamma C_{N\dot{\alpha}}$:

$$C_{Y_{\dot{\phi}}} = \delta\left[C_{N_q} + \gamma C_{N\dot{\alpha}}\right]$$
(10)

Determination of the Pitch-Damping Coefficients
The particular approach discussed here for determining the pitch-damping coefficients requires that the side force and moment due to coning ($C_{Y_{\dot{\phi}}}$ and $C_{n_{\dot{\phi}}}$) be determined. By computing the side force and moment for at least two different coning rates, the variation of side force and moment can be determined. If steady combined spinning and coning motion is used, the pitch-damping coefficients are easily determined because these coefficients are directly proportional to the side force and moment due to coning as shown in Eqs. (8) and (10). On the other hand, if steady lunar coning motion is used, the Magnus force and moment must be determined from another source before the pitch-damping coefficients can be determined [Eqs. (7) and (9)]. Often the Magnus force and moment are small in relation to the pitch-damping coefficients and can be ignored when determining the pitch-damping coefficients from the side force and moment due to steady lunar coning motion.

Because many projectile and missile applications deal with small amplitude motions, it is customary to linearize the equations of motion. Thus, the pitch-damping force and moment coefficients often appear as $C_{N_q} + C_{N\dot{\alpha}}$ and $C_{m_q} + C_{m\dot{\alpha}}$ because the cosine

of the angle of attack γ is nearly 1. This notation is adopted in the remainder of this paper.

Finally, because the results were obtained using steady motions, the two types of coning motion are referred to as lunar coning motion and combined spinning and coning motion in later sections with the understanding that these are, in fact, steady motions.

Computational Approach

Computation of the viscous flowfield about the axisymmetric shell configurations was accomplished by solving the thin-layer Navier–Stokes equations using a PNS technique. The computations were performed in a coordinate frame that rotates at the coning rate of the projectile. The fluid flow relative to the rotating coordinate frame does not vary with time, allowing the steady (non-time-varying) Navier–Stokes equations to be applied. The solution of the steady Navier–Stokes equations can be performed at a reasonable computational cost. The steady, thin-layer Navier–Stokes equations in cylindrical coordinate form are

$$\frac{\partial \hat{E}}{\partial \xi} + \frac{\partial \hat{E}}{\partial \eta} + \frac{\partial \hat{E}}{\partial \zeta} + \hat{H}_c + \hat{H} = \frac{1}{Re}\left(\frac{\partial \hat{S}}{\partial \zeta} + \hat{S}_c\right) \quad (11)$$

This form of the governing equations incorporates the effects of the centrifugal and Coriolis forces from the rotating coordinate frame through the source term $\hat{H}$. Each of these vectors are functions of the dependent variables represented by the vector $q^T = (\rho, \rho u, \rho v, \rho w, e)$. The inviscid flux and source terms are shown in Eq. (12). Details regarding the viscous terms $\hat{S}$ and $\hat{S}_c$ can be found in Refs. 8 and 12:

$$\hat{E} = \frac{1}{J}\begin{bmatrix} \rho U \\ \rho u U + \xi_x P \\ \rho v U \\ \rho w U \\ (e+P)U \end{bmatrix} \qquad \hat{F} = \frac{1}{J}\begin{bmatrix} \rho V \\ \rho u V + \eta_x P \\ \rho v V + \eta_\phi P/r \\ \rho w V + \eta_r P \\ (e+P)V \end{bmatrix}$$

$$\hat{G} = \frac{1}{J}\begin{bmatrix} \rho W \\ \rho u W + \zeta_x P \\ \rho v W + \zeta_\phi P/r \\ \rho w W + \zeta_r P \\ (e+P)W \end{bmatrix} \quad (12)$$

$$\hat{H}_c = \frac{1}{Jr}\begin{bmatrix} \rho w \\ \rho u w \\ 2\rho v w \\ \rho(w^2 - v^2) \\ (e+P)w \end{bmatrix} \qquad \hat{H} = \frac{1}{J}\begin{bmatrix} 0 \\ H_2 \\ H_3 \\ H_4 \\ H_5 \end{bmatrix}$$

where

$$H_2 = r\rho\Omega_c^2 \sin\alpha_t \cos\alpha_t \cos\phi - (x-x_{cg})\rho\Omega_c^2 \sin^2\alpha_t$$
$$+ 2\Omega_c \sin\alpha_t \cos\phi\rho v - 2\Omega_c \sin\alpha_t \sin\phi\rho w$$

$$H_3 = (x-x_{cg})\rho\Omega_c^2 \sin\alpha_t \cos\alpha_t \sin\phi + r\rho\Omega_c^2 \sin^2\alpha_t \cos\phi \sin\phi$$
$$+ 2\Omega_c \cos\alpha_t\rho w - 2\Omega_c \sin\alpha_t \cos\phi\rho u$$

$$H_4 = -r\rho\Omega_c^2 \sin^2\alpha_t \sin\phi - r\rho\Omega_c^2 \cos^2\alpha_t$$
$$+ (x-x_{cg})\rho\Omega_c^2 \sin\alpha_t \cos\alpha_t \cos\phi$$
$$+ 2\Omega_c \sin\alpha_t \sin\phi\rho u - 2\Omega_c \cos\alpha_t\rho v$$

$$H_5 = \left[-(x-x_{cg})\Omega_c^2 \sin^2\alpha_t \cos^2\alpha_t + r\Omega_c^2 \sin\alpha_t \cos\alpha_t \cos\phi\right]\rho u$$
$$+ \left[(x-x_{cg})\Omega_c^2 \cos\alpha_t \sin\alpha_t \sin\phi + r\Omega_c^2 \sin^2\alpha_t \cos\phi \sin\phi\right]\rho v$$
$$+ \left[(x-x_{cg})\Omega_c^2 \sin\alpha_t \cos\alpha_t \cos\phi\right]$$
$$- r\Omega_c^2 \sin^2\alpha_t \sin^2\phi - r\Omega_c^2 \cos^2\alpha_t\right]\rho w \quad (13)$$

$$U = u\xi_x \qquad V = u\eta_x + v\eta_\phi/r + w\eta_r$$
$$W = u\zeta_x + v\zeta_\phi/r + w\zeta_r \quad (14)$$

$$\xi_x = \frac{1}{x_\xi} \qquad \eta_x = J(r_\xi\phi_\zeta - \phi_\xi r_\zeta) \qquad \eta_\phi = J(x_\xi r_\zeta)$$

$$\eta_r = J(-x_\xi\phi_\zeta) \qquad \zeta_x = J(\phi_\xi r_\eta - r_\xi\phi_\eta) \quad (15)$$

$$\zeta_\phi = J(-x_\xi r_\eta) \qquad \zeta_r = J(x_\zeta\phi_\eta) \qquad J = \frac{1}{[x_\xi(\phi_\eta r_\zeta - \phi_\zeta r_\eta)]}$$

The pressure P can be related to the dependent variables by applying the ideal gas law,

$$P = (\gamma - 1)[e - (\rho/2)(u^2 + v^2 + w^2)] \quad (16)$$

The turbulent viscosity μ_t, which appears in the viscous matrices, was computed using the Baldwin–Lomax turbulence model.[13]

The thin-layer equations are solved using a PNS technique.[8] Following this approach, the governing equations, which have been modified here to include the Coriolis and centrifugal force terms, are solved using a conservative, approximately factored, implicit finite difference numerical algorithm.[14]

Following the approach of Ref. 8, the equations are first linearized and placed in delta form, where the equations are solved for the difference in the dependent variables rather than the variable itself. This set of equations is then factored using the approach of Ref. 14. The following set of equations is obtained:

$$\left[\tilde{A}_s^j + (1-\alpha)\Delta\xi\left(\delta_\eta\tilde{B}^j + \tilde{D}^j + \tilde{D}_c^j\right)\right]\Delta\hat{q}^* = \mathbf{RHS} \quad (17)$$

$$\left\{\tilde{A}^j + (1-\alpha)\Delta\xi\left[\delta_\zeta\tilde{C}^j - (1/Re)\left(\bar{\delta}_\zeta\tilde{M}^j + \tilde{M}_c^j\right)\right]\right\}\Delta\hat{q}^j$$
$$= \tilde{A}_s^j\Delta\hat{q}^* \quad (18)$$

$$\mathbf{RHS} = -\left(\tilde{A}_s^j - \tilde{A}_s^{j-1}\right)\hat{q}^j + \alpha\left(\hat{E}_s^j - \hat{E}_s^{j-1}\right) - \left[(\xi_x/J)^{j+1}E_p^j\right.$$
$$- (\xi_x/J)^j E_p^{j-1}\right] - (1-\alpha)\Delta\xi\left\{\delta_\eta\left[\eta_x^{j+1}(E/J)^j\right.\right.$$
$$+ (\eta_\phi/r)^{j+1}(F/J)^j + \eta_r^{j+1}(G/J)^j\right]$$
$$+ \delta_\zeta\left[\zeta_x^{j+1}(E/J)^j + (\zeta_\phi/r)^{j+1}(F/J)^j + \zeta_r^{j+1}(G/J)^j\right]$$
$$+ \hat{H}^j + \hat{H}_c^j - (1/Re)\left(\bar{\delta}_\zeta\tilde{S}^j + \tilde{S}_c^j\right) + \Phi\right\} \quad (19)$$

The form of the equations, as well as the notation, is similar to that used in Ref. 8, which should be consulted for additional details. The important difference here is the addition of the matrices $\tilde{D}$ and $\hat{H}$ due to the rotating coordinate system. Although the Jacobian matrix $\tilde{D}$ can be included in either the circumferential inversion or the normal inversion, including this term in the circumferential inversion simplifies slightly the implementation of the shock-fitting boundary conditions. Two additional Jacobian matrices, $\tilde{D}_c$ and $\tilde{M}_c$, appear in these equations and are due to the linearization of the inviscid and viscous cylindrical coordinate source terms $\hat{H}_c$ and $\hat{S}_c$.

The computations were performed using a shock-fitting procedure.[15] This procedure solves the five Rankine–Hugoniot jump conditions, two geometric shock-propagation conditions, and one compatibility equation to determine the values of the five dependent variables immediately behind the shock, as well as the position of the shock. By including the implicit part of the source term due to the rotating coordinate frame in the circumferential inversion, the existing shock-fitting procedure[15] can be used without modification, as long as the correct freestream conditions are specified as shown here in nondimensional form:

$$\rho = 1 \qquad \rho u = M_\infty \cos\alpha_t + r\Omega_c \sin\alpha_t \cos\phi$$

$$\rho v = M_\infty \sin\alpha_t \cos\phi - r\Omega_c \cos\alpha_t + (x-x_{cg})\Omega_c \sin\alpha_t \sin\phi$$

$$\rho w = M_\infty \sin\alpha_t \cos\phi - (x-x_{cg})\Omega_c \sin\alpha_t \cos\phi$$

$$e = 1/[\gamma(\gamma-1)] + \tfrac{1}{2}\left[M_\infty^2 + r^2\Omega_c^2\left(\sin^2\alpha_t \cos^2\phi + \cos^2\alpha_t\right)\right.$$
$$- 2r(x-x_{cg})\Omega_c^2 \cos\alpha_t \sin\alpha_t \sin\phi$$
$$+ (x-x_{cg})^2\Omega_c^2 \sin^2\alpha_t\right] \quad (20)$$

At the body surface, no-slip, constant wall temperature boundary conditions were applied. For the cases with spin, the circumferential velocity v was set equal to the local velocity of the body surface due to solid body rotation.

The computational results were obtained using a grid that consisted of 60 points between the body and the shock. In the circumferential direction, gridding was performed over a 360-deg sector because of the lack of symmetry from the combination of angle of attack, spin, and coning motion. In the circumferential direction, 36 grid points were used. In longitudinal direction, 78 marching steps were utilized for each body diameter of length. To ensure adequate grid resolution within the boundary layer, the grid spacing at the body surface was adapted to maintain nondimensional boundary-layer coordinate y^+ between 2 and 3 in accordance with previously published results.[16] Grid resolution studies showed less than 2% variation in the computed pitch-damping coefficient when the grid resolution was decreased by 25% in each of the three coordinate directions. Similarly, when the grid in the circumferential and marching directions was doubled and the grid in the radial direction was increased by 50%, the computed pitch-damping coefficient varied by only 1%. The computations for the baseline grid performed using a Cray Y-MP supercomputer typically required less than 10 min of CPU time for complete calculation over a single configuration.

Results

Computations were performed to determine the aerodynamics of several axisymmetric shell configurations in steady coning motion. The first set of predictions is for two generic shell configurations: an SOC and an SOCBT. Calculations were performed over a range of Mach numbers and body lengths. The PNS results were compared with Euler code results. A second set of results was obtained for a series of ogive-cylinder configurations [Army–Navy spinner rocket (ANSR)], which were fired through an aerodynamics range located at the former Ballistic Research Laboratory. The computational results are compared with the aerodynamics determined from the in-flight motion of the projectile.

Results for the SOC and SOCBT

A schematic of the SOCBT configuration is shown in Fig. 2. The SOC is identical to the SOCBT configuration except that the boattail is replaced by a cylinder. The PNS results were compared with pitch-damping results obtained using an inviscid code.[4] Results were obtained for three body lengths (5, 6, and 7 calibers) and a range of supersonic Mach numbers. The c.g. position used in the calculations was located at 60% of the body length from the nose. The PNS results were obtained using the combined spinning and coning motion approach. The Euler results were obtained using lunar coning motion because the spin boundary condition required by the combined spinning and coning motion is incompatible with the requirement for zero shear at the body surface in the inviscid approach.

Figures 3 and 4 show the variation of the pitch-damping moment coefficient as a function of Mach number for the three body lengths. In the supersonic regime, the pitch-damping moment shows a decreasing trend with increasing Mach number. The inviscid results at $L/D = 7$ show a maximum near Mach 2. The results also show a significant increase in the pitch-damping moment with increasing
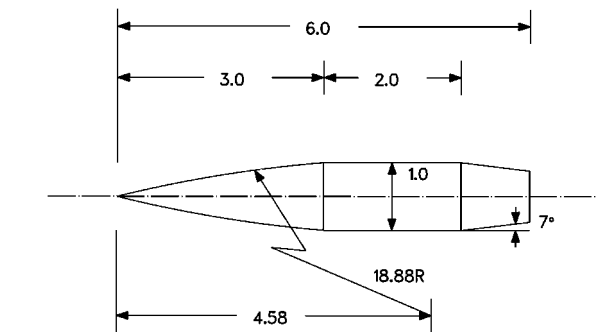

Fig. 2 Schematic of the SOCBT configuration. All dimensions are in calibers (one caliber = 57.2 mm).
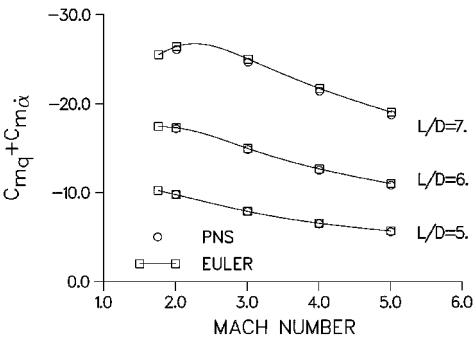

Fig. 3 Pitch-damping moment coefficient vs Mach number for various body lengths, SOC configuration.
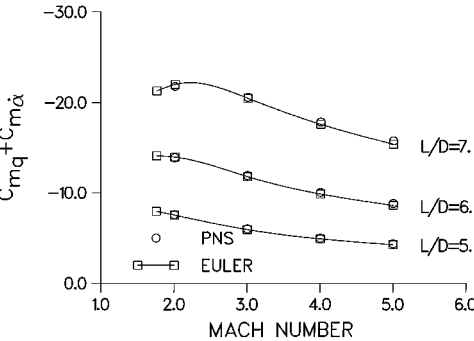

Fig. 4 Pitch-damping moment coefficient vs Mach number for various body lengths, SOCBT configuration.

body length. The effect of the boattail is to reduce the pitch-damping moment by 20–30% compared with the cylindrical afterbody.

The comparison of the pitch-damping moment predictions from the PNS approach and the Euler approach shows differences of less than 4% across the range of parameters considered. The small differences between PNS and Euler predictions are not surprising because the pitch damping appears to be primarily an inviscid phenomenon. However, the degree of agreement between the PNS and inviscid code is not an absolute indicator of the magnitude of viscous effects because there does appear to be some code-to-code variation of the predicted pitch damping, which is on the order of the viscous effect. The relevance of these differences is probably not significant, especially in light of difficulties in measuring this coefficient experimentally.

The PNS predictions shown earlier were obtained using the combined spinning and coning motion. This motion allows the pitch-damping force and moment to be determined directly from the side force and moment. As already mentioned, the accuracy of this approach depends on the degree to which the Magnus moment is accurately predicted. In previous studies, a numerical capability for determining Magnus force and moment at small angles of attack has been already established.[16] This capability is based on the same numerical approach as applied here.

Figure 5 shows predictions of the Magnus moment coefficient for the SOCBT configuration. The Magnus moment for the SOC configuration is about 70–80% of the SOCBT Magnus moment. The expected differences between using lunar coning motion and combined spinning and coning motion to determine the pitch-damping moment is the Magnus moment coefficient. For the cases examined here, the Magnus moment is less than 4% of the pitch-damping coefficient. The biggest differences were observed for the boattailed configuration, which has a larger Magnus moment and a smaller pitch-damping moment than the SOC configuration. Thus, using lunar coning motion and ignoring the Magnus moment contribution still yields accurate values of the pitch-damping coefficient for the configurations and conditions under consideration here.

The predicted variation of the pitch-damping force coefficient with Mach number for the SOC configuration is shown in Fig. 6. These results were obtained from the side force due to combined spinning and coning motion. The results show a strong decrease
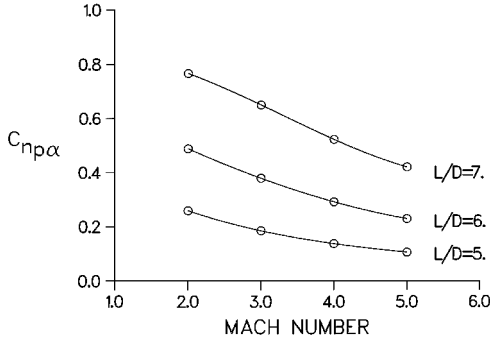
Fig. 5 Magnus moment coefficient vs Mach number for various body lengths, SOCBT configuration.
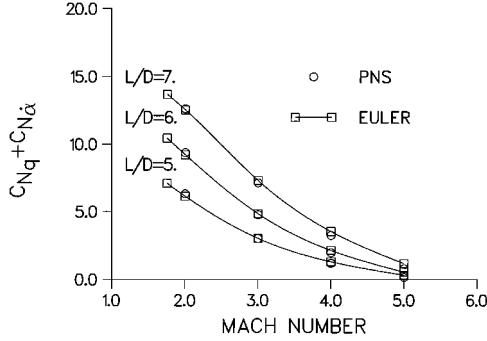

Fig. 6 Pitch-damping force coefficient vs Mach number for various body lengths, SOC configuration.

in the coefficient with increasing Mach number across the range of parameters examined. The results also show an increase in the coefficient with increasing body length. The PNS and Euler results are in good agreement.

Results for the ANSR

Computations were performed for the ANSR series of projectiles. These projectiles were fired in an aerodynamics range, and the aerodynamics determined from the projectile motion.[17] The projectiles consisted of a 2-caliber ogive nose with several different length cylindrical bodies, as shown in Fig. 7. The total body lengths were 5, 7, and 9 calibers. For each body length, projectiles were fabricated and fired with three different c.g. locations. The use of projectiles with different c.g. locations allowed the aerodynamic forces to be determined from the variation of the aerodynamic moments with c.g. location.

Figures 8 and 9 show the variation of the pitch-damping moment coefficient with c.g. location for the 5-, 7-, and 9-caliber bodies at Mach 1.8 and Mach 2.5, respectively. In Figs. 8 and 9, the computed results are compared with the experimental measurements. The computational results are considered to be within the accuracy of the experimental measurement and are typically bracketed by the experimental data. For each body length, computations were performed at each of three c.g. locations. Because the body rotates about the c.g., each computation produced a unique flowfield and pitch-damping coefficient. These results are displayed by the triangular symbols in both figures. As well, once the aerodynamics of a given configuration are determined, the c.g. translation relations[1] can be applied to predict the aerodynamic coefficients for the same configuration with a different c.g. location. Several of these relations are shown as follows:

$$\hat{C}_{N_\alpha} = C_{N_\alpha} \qquad \hat{C}_{m_\alpha} = C_{m_\alpha} - s_{cg} C_{N_\alpha}$$

$$\hat{C}_{N_q} + \hat{C}_{N_{\dot\alpha}} = C_{N_q} + C_{N_{\dot\alpha}} + s_{cg} C_{N_\alpha} \qquad (21)$$

$$\hat{C}_{m_q} + \hat{C}_{m_{\dot\alpha}} = C_{m_q} + C_{m_{\dot\alpha}} - s_{cg}\left(C_{N_q} + C_{N_{\dot\alpha}}\right) + s_{cg} C_{m_\alpha} - s_{cg}^2 C_{N_\alpha}$$

The aerodynamic coefficients for the modified configuration are denoted by the caret, whereas the aerodynamic coefficients for the
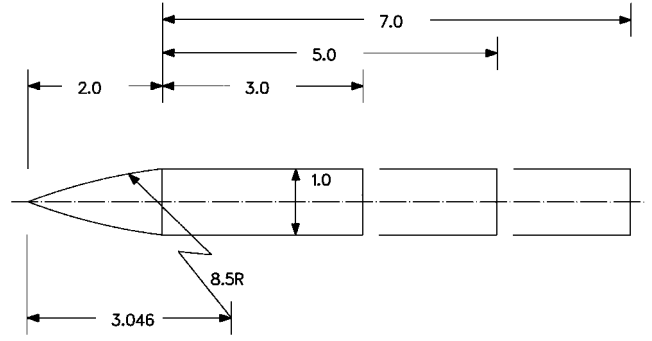

Fig. 7 Schematic of the ANSR. All dimensions are in calibers (one caliber = 20 mm).
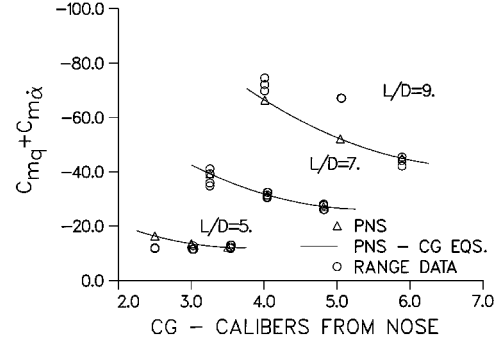

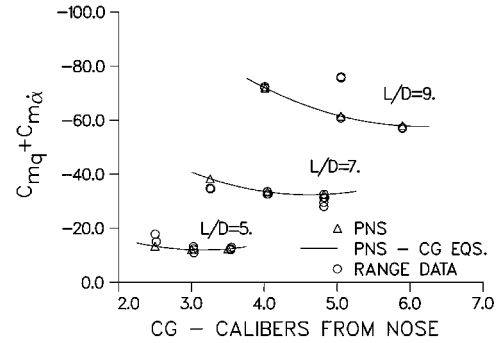Fig. 8 Pitch-damping moment coefficient vs c.g. location, Mach 1.8, ANSR.

Fig. 9 Pitch-damping moment coefficient vs c.g. location, Mach 2.5, ANSR.

baseline configuration are shown on the RHS of the equations. The c.g. shift s_{cg} is in calibers and is positive for a c.g. shift toward the nose. Using these relations and the predicted aerodynamic coefficients for the middle c.g. position, the variation of the pitch-damping moment coefficient with c.g. location was determined. This variation is shown in Figs. 8 and 9 by the solid line. The difference between the pitch-damping moment coefficients predicted from the c.g. translation relations and determined from the direct computations is less than 0.1%. The agreement between the two approaches serves as a consistency check for the computational approach.

It is noted that at both Mach numbers, for the middle c.g. position of the 9-caliber body, there are several experimental data points that deviate from the trend shown by the predictions and the apparent trend shown by the experimental data. The cause of this deviation is unknown.

As seen from the c.g. translation relations, C_{m_α} varies linearly with the c.g. shift. The slope of the variation is the normal force coefficient slope C_{N_α}. By firing projectiles with the same external shape but with different c.g. positions, C_{N_α} can be determined from the variation of C_{m_α} with c.g. location. A similar approach can be used to determine the pitch-damping force coefficient from the variation of the pitch-damping moment coefficient with c.g. location. Because the pitch-damping moment varies in a nonlinear fashion with the c.g. shift, a modified damping moment is defined as

$$\hat{C}_{m_q} + \hat{C}_{m_{\dot\alpha}} - s_{cg}\hat{C}_{m_\alpha} = C_{m_q} + C_{m_{\dot\alpha}} - s_{cg}\left(C_{N_q} + C_{N_{\dot\alpha}}\right) \quad (22)$$

When the left-hand side of this equation is plotted as a function of c.g. shift, the results should be a line with slope equal to the pitch-damping force coefficient. For all practical purposes, the determination of the pitch-damping force from range firings can only be obtained from the variation of the pitch-damping moment with c.g. locations because the pitch-damping force coefficient contributes little to the in-flight motion of the projectile. Hence, direct determination is not practical.

From the c.g. variation of the pitch-damping moment, the pitch-damping force coefficient was determined from the experimental measurements. Figure 10 shows the variation of the pitch-damping force coefficient with body length for the middle c.g. location. Note that, unlike the normal force coefficient, the pitch-damping force varies with c.g. position. The agreement between the computational predictions and experimental results are within the experimental accuracy and show the correct variation with body length and Mach number.

As mentioned, the pitch-damping predictions were obtained using the combined spinning and coning motion, which allows the pitch-damping force and moment to be determined directly from the side force and moment. The expected differences between applying combined spinning and coning motions and lunar coning motion are reflected in the Magnus moment coefficient. In the current effort, the Magnus force and moment have been computed for the ANSR configuration and comparison made with range data obtained from the same series of firings, as shown in Figs. 11 and 12. The computed

results were obtained for a fully turbulent boundary layer, although there is some evidence from the experimental program to indicate laminar flow over a portion of the body, particularly near the nose. The computational results are within the scatter of the experimental data for most of the c.g. positions although several of the cases show an overprediction by as much as 30–40%. The predictions show that determining the pitch-damping coefficient directly from the side moment due to lunar coning motion (which requires the Magnus moment to be ignored) will result in errors of less than 5% for this configuration.

Finally, using the Magnus results and the side force and moment due to lunar coning motion, predictions of the pitch-damping coefficients [Eqs. (7) and (9)] were made and compared with the predictions of the pitch-damping coefficients obtained using a single calculation utilizing combined spinning and coning motion. The maximum difference between the two approaches was less than 0.1%, demonstrating the lack of coupling between spinning and coning motions over the range of coning rates, spin rates, and angles of attack considered. (It is interesting to note that at higher angles of attack, a nonlinear variation of Magnus moment with angle of attack was predicted. Even at these angles of attack, no coupling between the coning and spinning motions was observed.)

Conclusion

A computational approach for predicting the pitch-damping coefficients using steady coning motion has been successfully applied to several axisymmetric shell configurations. Through the use of a combined spinning and coning motion, the pitch-damping force and moment have been obtained directly from the side force and moment using a single calculation. This approach does not require that the Magnus force or moment be ignored or determined from an auxiliary calculation, as in the case of lunar coning motion.

The computational predictions for the SOC and SOCBT configurations showed good agreement with results obtained with a previously published inviscid code. The results showed an increasing trend in the pitch-damping coefficient with increasing length-to-diameter ratio and a decreasing trend in the coefficient with increasing Mach number. The presence of the boattail on the projectile produced a significant reduction in the pitch-damping moment compared with an equivalent length cylindrical afterbody. The predictions of the pitch-damping force and moment coefficients for the ANSR were seen to be in excellent agreement with the data obtained from aerodynamic range testing. The computational results predicted the correct variation in the pitch-damping moment coefficient with changing c.g. location, body length, and Mach number. For each of the configurations examined, the effect of viscosity on the pitch-damping coefficients was small.

The use of the combined spinning and coning motion is currently being applied to time-marching codes for the prediction of pitch-damping at subsonic through low supersonic velocities. In this velocity regime, it is expected that viscous effects will be of greater importance than in the supersonic regime.

Fig. 10   Pitch-damping force coefficient vs body length, middle c.g. location, ANSR.

Fig. 11   Magnus moment coefficient vs c.g. location, Mach 1.8, ANSR.

Fig. 12   Magnus moment coefficient vs c.g. location, Mach 2.5, ANSR.

References

[1] Murphy, C. H., "Free Flight Motion of Symmetric Missiles," U.S. Army Ballistic Research Lab., Rept. 1216, Aberdeen Proving Ground, MD, July 1963.

[2] Tobak, M., Schiff, L. B., and Peterson, V. L., "Aerodynamics of Bodies of Revolution in Coning Motion," *AIAA Journal*, Vol. 7, No. 1, 1969, pp. 95–99.

[3] Schiff, L. B., and Tobak, M., "Results from a New Wind-Tunnel Apparatus for Studying Coning and Spinning Motions of Bodies of Revolution," *AIAA Journal*, Vol. 8, No. 11, 1970, pp. 1953–1957.

[4] Schiff, L. B., "Nonlinear Aerodynamics of Bodies in Coning Motion," *AIAA Journal*, Vol. 10, No. 11, 1972, pp. 1517–1522.

[5] Agarwal, R., and Rakich, J. V., "Computation of Supersonic Laminar Viscous Flow Past a Pointed Cone at Angle of Attack in Spinning and Coning Motion," AIAA Paper 78-1211, July 1978.

[6] Lin, T. C., "A Numerical Study of the Aerodynamics of a Reentry Vehicle in Steady Coning Motion," AIAA Paper 78-1358, Aug. 1978.

[7] Weinacht, P., and Sturek, W. B., "Navier–Stokes Predictions of Pitch Damping for Finned Projectiles Using Steady Coning Motion," *Proceedings of the AIAA 8th Applied Aerodynamics Conference*, AIAA, Washington, DC, 1990, pp. 632–642 (AIAA Paper 90-3088).
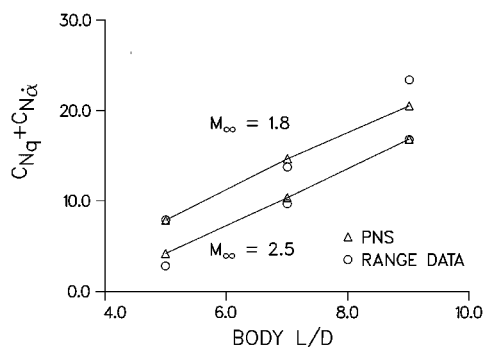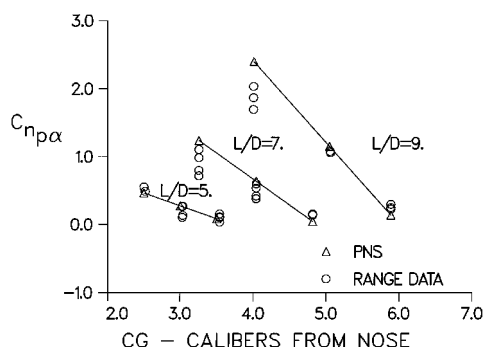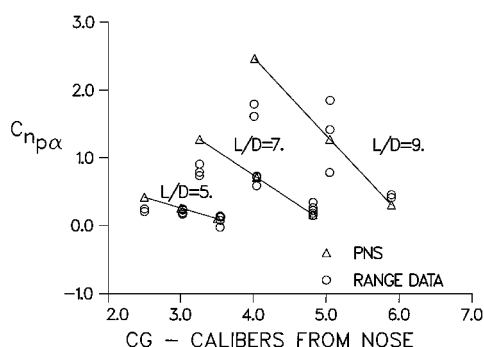
[8]Schiff, L. B., and Steger, J. L., "Numerical Simulation of Steady Supersonic Viscous Flow," *AIAA Journal*, Vol. 18, No. 12, 1980, pp. 1421–1430.

[9]Levy, L. L., and Tobak, M., "Nonlinear Aerodynamics of Bodies of Revolution in Free Flight," *AIAA Journal*, Vol. 8, No. 12, 1970, pp. 2168–2171.

[10]Tobak, M., and Schiff, L. B., "Generalized Formulation of Nonlinear Pitch-Yaw-Roll Coupling: Part I—Nonaxisymmetric Bodies," *AIAA Journal*, Vol. 13, No. 3, 1975, pp. 323–326.

[11]Tobak, M., and Schiff, L. B., "Generalized Formulation of Nonlinear Pitch-Yaw-Roll Coupling: Part II—Nonlinear Coning Rate," *AIAA Journal*, Vol. 13, No. 3, 1975, pp. 327–332.

[12]Weinacht, P., and Sturek, W. B., "Computation of the Roll Characteristics of a Finned Projectile," *Journal of Spacecraft and Rockets*, Vol. 33, No. 6, 1996, pp. 769–775.

[13]Baldwin, B. S., and Lomax, H., "Thin Layer Approximation and Algebraic Model for Separated Turbulent Flows," AIAA Paper 78-257, Jan. 1978.

[14]Beam, R., and Warming, R. F., "An Implicit Factored Scheme for the Compressible Navier–Stokes Equations," *AIAA Journal*, Vol. 16, No. 4, 1978, pp. 393–402.

[15]Rai, M. M., and Chaussee, D. S., "New Implicit Boundary Procedure: Theory and Applications," AIAA Paper 83-0123, Jan. 1983.

[16]Sturek, W. B., and Schiff, L. B., "Computations of the Magnus Effect for Slender Bodies in Supersonic Flight," *Proceedings of the AIAA Atmospheric Flight Mechanics Conference*, AIAA, New York, 1980, pp. 260–280 (AIAA Paper 80-1586).

[17]Murphy, C. H., and Schmidt, L. E., "The Effect of Length on the Aerodynamics Characteristics of Bodies of Revolution in Supersonic Flight," U.S. Army Ballistic Research Lab., Rept. 876, Aberdeen Proving Ground, MD, Aug. 1953.

R. M. Cummings
Associate Editor